

## Research Article

# Mixed Mode I-II Fracture Path and Initiation Angle of Concrete at Mesoscale Level

Guodong Li <sup>1,2</sup>, Zhengyi Ren,<sup>1,2</sup> Zhiyuan Wang <sup>1,2</sup>, Jiangjiang Yu,<sup>1,2</sup>  
and Zhimeng Zhao<sup>1,2</sup>

<sup>1</sup>Transportation Institute, Inner Mongolia University, Hohhot, China

<sup>2</sup>Inner Mongolia Engineering Research Center of Testing and Strengthening for Bridges, Hohhot, China

Correspondence should be addressed to Zhiyuan Wang; nmgzyh0845@163.com

Received 14 December 2018; Revised 22 March 2019; Accepted 1 April 2019; Published 6 May 2019

Academic Editor: Hiroshi Yoshihara

Copyright © 2019 Guodong Li et al. This is an open access article distributed under the Creative Commons Attribution License, which permits unrestricted use, distribution, and reproduction in any medium, provided the original work is properly cited.

This paper presents the mesoscale numerical simulation and experimental verification of mixed mode I-II fracture for the four-point shearing beam with a single-side notch based on the concrete damaged plasticity (CDP) method and the Monte Carlo simulation (MCS) random aggregate method. And it discusses the influence of volume rate and maximum size of the coarse aggregate on the fracture path and the initiation angle of concrete mixed mode I-II fracture. The results show that the coarse aggregate has a significant influence on the distribution width, average length, and the dispersion degree of the fracture path, the distribution of which can be fitted by a normal distribution function. Also, the distribution width of the fracture path has a quadratic function relationship with the height along the failure direction. The distribution of coarse aggregates at the top of the reserved notch also has a significant influence on the initiation angle, which determines the initiation crack direction of mixed mode I-II fracture in concrete. The initiation angle distributes near the failure direction and follows a normal distribution function.

## 1. Introduction

Cracks occur and develop during the whole life of concrete materials from the pouring stage, construction stage, and use stage to failure stage. The failure process of concrete is different from brittle materials such as glass due to the inhomogeneity. And the fracture process of concrete at the mesoscale appears as microcrack initiation, expansion, and penetration until the macrofracture [1, 2]. The asymmetric loading in practical engineering structure directly determines that the initiation and expansion behaviors of cracks are not simply mode I (opening mode), mode II (sliding mode), or mode III (tearing mode), but the different combinations of these three modes. Also, the stress state of mode I that most likely causes failure is avoided due to the concrete structure design so that the frequency of mixed mode I-II fracture increases. Therefore, the whole process of mixed mode I-II fracture has become the engineering problem generally concerned by scholars [3, 4].

Concrete is one kind of heterogeneous composite material consisting of cement mortar, coarse aggregates, mortar-

aggregate interface, and pores at the mesoscale [5–8], and the volume rate of the coarse aggregate in concrete is about 60% to 70% [9, 10]. A large number of studies have shown that the gradation, volume rate, and maximum size of coarse aggregate have a significant influence on the fracture properties and fracture parameters of concrete [11–14]. It is difficult to reveal the influence of the coarse aggregate on the whole process for the microcrack generation, aggregation, development, and fracture during the experimental procedure at mesoscale. And the numerical simulation method makes up for the deficiency of the experiment. However, most of the existing studies are based on the mode I fracture of concrete. It is more consistent with the composite stress state in actual engineering structure to discuss the influences of the volume rate and maximum size of the coarse aggregate on the mixed mode I-II fracture properties of concrete. And it can more effectively analyze the damage, the fracture mechanism, and the crack resistance of concrete to propose methods for improving the fracture properties of concrete.

The influences of the volume rate and maximum size of the coarse aggregate and the size effect of the specimen on

the mechanical properties of mixed mode I-II fracture in concrete have been discussed [15, 16]. In this paper, the influences of the volume rate and maximum size of the coarse aggregate on the fracture path and the initiation angle for mixed mode I-II fracture in concrete were investigated based on the experimental results and the random aggregate numerical simulation results of seven working conditions. And seven kinds of concrete with different coarse aggregate were designed, among which, the volume rates were 0%, 29%, 48%, and 68%, and the maximum particle sizes were 9.5 mm, 19 mm, and 26.5 mm.

## 2. Experimental Process and Methods

**2.1. Concrete Materials and Mix Proportions.** The cementitious materials used in this study included P.O 42.5 ordinary Portland cement (strength grade 42.5 MPa) and fly ash (I-type high-calcium ash), both from Inner Mongolia and China. River sand with a particle size range from 0.30 mm to 4.75 mm was used as the fine aggregate. And three-grade continuous gradation mechanical crushed granite stone with a particle size of 4.75 mm to 9.5 mm, 9.5 mm to 19 mm, and 19 mm to 26.5 mm was selected as the coarse aggregate, as shown in Figure 1. The aggregate was mixed according to the mix proportions requirements. The polycarboxylate superplasticizer with a water reducing rate of 30% was used to improve the workability of concrete. The mix proportions and the parameters of concrete materials have been shown in the paper [15].

In order to highlight the influence of the volume rate of the coarse aggregate on mixed mode I-II fracture properties of concrete, four kinds of mix proportions with the volume rates of the coarse aggregate of 0%, 29%, 48%, and 68% were designed while the proportions of each part of the materials in mortar and the coarse aggregate gradation were kept consistent. Considering the influence of the maximum size of the coarse aggregate on mixed mode I-II fracture properties of concrete, three kinds of mix proportions with the maximum size of the coarse aggregate of 9.5 mm, 19 mm, and 26.5 mm were designed, while the cement mortar and the coarse aggregate volume rate kept unchanged. The water-cement ratio of concrete was 0.34, and the slump was controlled at  $180 \pm 20$  mm. The curing conditions for all of the specimens was with a temperature of  $20 \pm 2^\circ\text{C}$ , humidity was above 95%, and the experimental age of the concrete was 90 days.

**2.2. Experimental Methods.** In this paper, the specimen of the mixed mode I-II fracture experiment was a single-side notched four-point shearing beam with a size of  $320 \text{ mm} \times 160 \text{ mm} \times 80 \text{ mm}$ . A larger specimen was cut and processed into multiple beams, which can observe the distribution of the coarse aggregate on the two sides of the beam. The mixed mode I-II fracture was induced by cutting a through-notch with a section size of  $3 \text{ mm} \times 32 \text{ mm}$  at the bottom of the beam and applied a four-point shearing anti-symmetric load. The load provided by MTS was consistent with the midline of the beam and transmitted to the concrete beam through a rigid beam. The location of the loading points

is shown in Figure 2. The loading process was controlled by the displacement rate of 0.0003 mm/s.

## 3. Numerical Simulation of Four-Point Shearing Experimental

**3.1. Concrete Damaged Plasticity Model of Cement Mortar.** The concrete damaged plasticity (CDP) model proposed by Lee and Fenves [17, 18] has been quite mature in commercial finite element software such as ABAQUS, and it has been proved that the CDP model can adequately reflect the damage and fracture process of concrete [19–24]. In this paper, the concrete is studied as a composite material composed of cement mortar, aggregate, and pores. Additionally, it is assumed that the coarse aggregate is always in the linear elastic stage during the loading process without damage, and only the cement mortar unit is given the concrete damaged constitutive plasticity properties.

Similar to the classical plastic theory, the CDP model divides the total strain into the elastic part and the plastic part, as shown in the following equation:

$$\varepsilon = \varepsilon^{\text{el}} + \varepsilon^{\text{pl}}, \quad (1)$$

where  $\varepsilon$  is the total strain,  $\varepsilon^{\text{el}}$  is an elastic strain, and  $\varepsilon^{\text{pl}}$  is a plastic strain.

The CDP model connects the damaged state and the undamaged state by defining the damage variable  $d$  which can take the value from 0 (undamaged) to 1 (completely damaged). The following equation is the stress-strain relation in the CDP model:

$$\sigma = (1 - d)D_0^{\text{el}} : (\varepsilon - \varepsilon^{\text{pl}}) = D^{\text{el}} : (\varepsilon - \varepsilon^{\text{pl}}). \quad (2)$$

Effective stress:

$$\bar{\sigma} = D_0^{\text{el}} : (\varepsilon - \varepsilon^{\text{pl}}), \quad (3)$$

where  $D_0^{\text{el}}$  is the initial nondestructive stiffness of the material.

And the yield function defined by the effective stress is as follows [17, 18, 25]:

$$F(\bar{\sigma}, \tilde{\varepsilon}^{\text{pl}}) = \frac{1}{1 - \alpha} (\bar{q} - 3\alpha\bar{p} + \beta(\tilde{\varepsilon}^{\text{pl}}) \langle -\hat{\sigma}_{\text{max}} \rangle - \gamma \langle -\hat{\sigma}_{\text{max}} \rangle) - \bar{\sigma}_c(\tilde{\varepsilon}_c^{\text{pl}}) \leq 0, \quad (4)$$

where  $\alpha = (f_{b0}/f'_c - 1)/(2f_{b0}/f'_c - 1)$ ,  $\beta = (\bar{\sigma}_c(\tilde{\varepsilon}_c^{\text{pl}})/\bar{\sigma}_t(\tilde{\varepsilon}_t^{\text{pl}})) / (1 - \alpha) - (1 + \alpha)$ ,  $\gamma = 3(1 - K_c)/(2K_c - 1)$ ,  $\langle x \rangle = (|x| + x)/2$ ,  $\bar{p}$  is effective hydrostatic pressure,  $\bar{q}$  is Mises equivalent stress,  $\alpha$  and  $\gamma$  are dimensionless parameters,  $\hat{\sigma}_{\text{max}}$  is the maximum principal stress,  $f_{b0}/f'_c$  is the ratio of the compressive strength under biaxial loading to uniaxial compressive strength, and  $K_c$  is the ratio of the second stress invariant on the tensile meridian to that on the compressive meridian at initial yield for any given value of the pressure invariant.

In the process of plastic deformation, the direction of plastic deformation and the evolution process of tension/

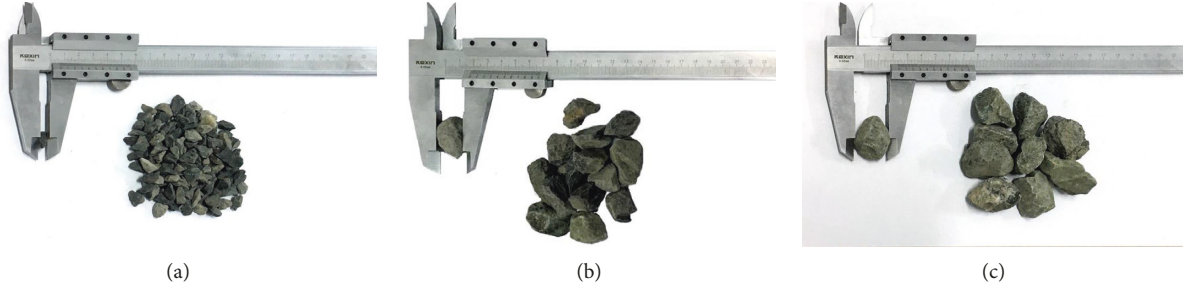


FIGURE 1: Coarse aggregate appearance with different sizes. (a) 4.75 mm~9.5 mm. (b) 9.5 mm~19 mm. (c) 19 mm~26.5 mm.

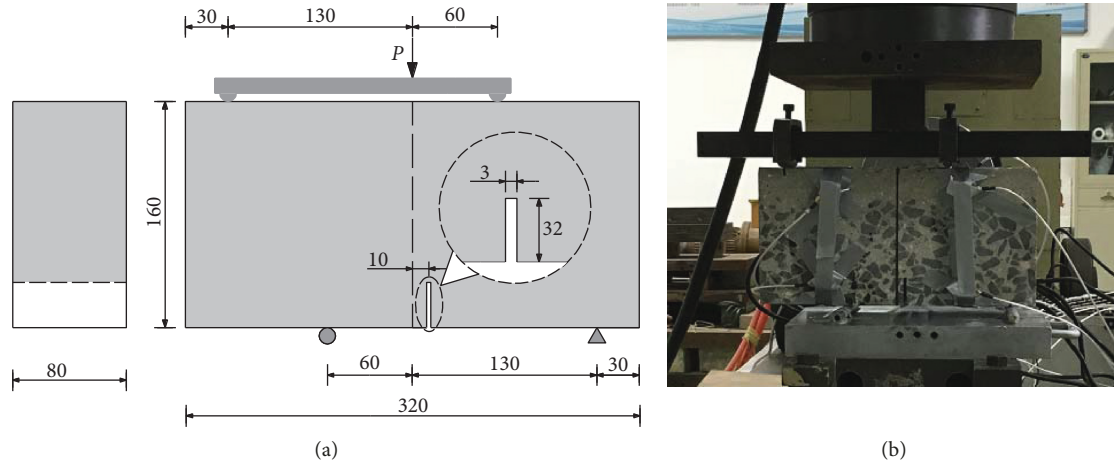


FIGURE 2: Test loading arrangement.

compression strain increments are determined by the flow law:

$$G = \sqrt{(e\sigma_{t0} \tan \psi)^2 + \bar{q}^2} - \bar{p} \tan \psi, \quad (5)$$

where  $e$  is the eccentricity,  $\sigma_{t0}$  is the uniaxial tensile stress at failure, and  $\psi$  is the dilation angle.

The parameters to be defined in the CDP model in this study are shown in Table 1 [26, 27].

**3.2. Four-Point Shearing Beam Model Based on the Random Aggregate Method.** For further research of the influences of volume rate and maximum particle size for coarse aggregate on the mixed mode I-II fracture characteristics of concrete, the two-dimensional random aggregate finite-element mesoscopic model of concrete is established based on concrete damage plasticity model and Monte Carlo simulation (MCS) method.

This paper adopted the random variable uniformly distributed on  $[0, 1]$  to describe the random distribution characteristics of coarse aggregate, and the probability density function of the random variable  $x$  is

$$f(x) = \begin{cases} 1, & x \in [0, 1], \\ 0, & x \in [0, 1], \end{cases} \quad (6)$$

$\{x_n\}$  is the sampling sequence of the random variable  $x$  and  $x_n$  is the random number of the randomly distributed

TABLE 1: CDP model parameters.

$\psi$	$e$	$f_{b0}/f'_c$	$K_c$	Coefficient of viscosity
$33^\circ$	0.1	1.16	0.667	0

random variable  $x$  on the interval of  $[0, 1]$ . The random numbers are generated by mathematical methods following the mathematical recurrence rule, and the recurrence formula is as follows:

$$x_n = f(x_{n-1}, x_{n-2}, \dots, x_{n-k}). \quad (7)$$

Once the random number  $i$  is determined, the random number  $i + 1$  is also determined. In that case, these random number sequences can only be regarded as real random numbers through a series of statistical tests. The mixed congruence method is used to generate the random numbers on  $[0, 1]$ ; the formula is as follows:

$$\begin{cases} X_n = \text{mod}(\lambda X_{n-1} + C, M), \\ R_n = X_n M^{-1}. \end{cases} \quad (8)$$

In this study, the random distribution center coordinates and extension radius of aggregate particles are used as the control parameters to generate convex polygon random aggregate base on the inner polygon of circular aggregate, the MATLAB software programming is used to achieve the random placement of coarse aggregate, and the flow chart of random aggregate generation is shown in Figure 3.

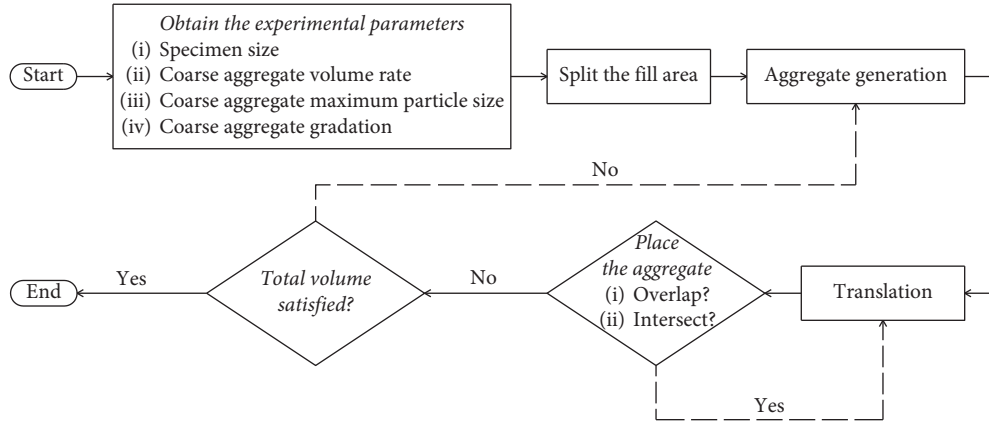


FIGURE 3: Flow chart of random aggregate generation.

The ABAQUS is used to realize the mesh generation and calculate the nonlinear fracture behavior of the models. The 3-node continuum plane stress element (CPS3) with a thickness of 80 mm (consistent with the thickness of the experiment beam) is used in this model, and the model size is 320 mm × 160 mm with a reserved notch size of 3 mm × 32 mm. The loading points are simulated by four rigid analytical bodies, each of which is coupled with independent reference points and different boundary conditions. The contact form between the restrained rigid body and concrete model is rigid contact with a friction coefficient of 0.2. The mix proportions of the models were consistent with the actual proportion of the experimental specimens, and the number of elements in each model was set at about 20,000. For each mix proportion of concrete, 350 finite element models are generated corresponding to seven working conditions to ensure the convergence of the statistical results. The displacement load of all models is the same, and the analysis time of the dynamic analysis is 0.1 s. The position and action mode of the loading points are precisely the same as Figure 2. The details and process of the model establishment have been comprehensively described in the references [15, 16], and the calculation results of the models have been verified with the experimental results in terms of mechanical properties, deformation, and failure morphology. The concrete schematic diagram of the models is shown in Figures 4 and 5.

## 4. Results and Discussion

**4.1. Fracture Path.** To study the influences of the volume rate and maximum size of coarse aggregate on the distribution width of the fracture path for mixed mode I-II fracture in concrete, the direction between crack initiation and termination is defined as failure direction in this paper. Furthermore, a coordinate system is established as shown in Figure 6(a), the origin of the coordinate is at the top of the reserved notch, the  $X$ -axis represents the distribution width of the fracture path, and the  $Y$ -axis is along the failure direction. In the numerical simulation results, the distribution position of each fracture path is different, and the upper and lower limits of the distribution width in each fracture path are divided into a damaged band as shown in Figure 7(b).

According to this, a line is added along the  $X$ -axis to calculate the damage probability at different  $X$  values, and the results are shown in Figure 7(c). The data analysis shows that the damage probability at different  $X$  values obeys the normal distribution function (equation (9)), and the correlation coefficients  $r$  of the data fitting are all greater than 0.95. To meet the requirement of 95% guarantee rate in engineering, this study takes the width of local coordinate system  $4\sigma$  as the effective width of fracture path distribution which is defined as the “damaged band” for the convenience of description:

$$f(x) = \frac{1}{\sqrt{2\pi}\sigma} e^{-\frac{(x-\mu)^2}{2\sigma^2}}, \quad (9)$$

where  $\mu$  is the average value and  $\sigma$  is the standard deviation.

Figure 6(a) presents the distribution width of the fracture path and the damage bandwidth of each specimen with different coarse aggregate volume rate. With the increases of the volume rate of coarse aggregate, the distribution width of the fracture path and the damaged bandwidth become wider, the spatial distribution of fracture paths becomes more discrete, and the average length of the fracture path becomes longer (as shown in Figure 6(c)). It is clear that with the increases of the volume rate, the number of distributes of the coarse aggregate in the failure direction increases and the randomness of distribution for coarse aggregate also increases. As a result, the distribution of the fracture path becomes more discrete. Although the distribution position of the coarse aggregate is different in the fracture direction, the overlap of coarse aggregate in the direction of  $X$  increases; there are two modes of the fracture path: (1) bypassing these coarse aggregates, respectively, and selecting the broken line path to expand; (2) extending around the outer edge of these coarse aggregates. The fracture path of the model (1) is longer and requires more energy consumption. And the fracture path statistical result shows that the model (2) is the primary form of fracture propagation. Therefore, with the increases of the coarse aggregate volume rate, the distribution width of the fracture path and the damaged bandwidth increase and the length of the fracture path increases.

Figure 6(b) shows the distribution width of the fracture path and the damaged bandwidth of each specimen with different coarse aggregate maximum particle size. It was

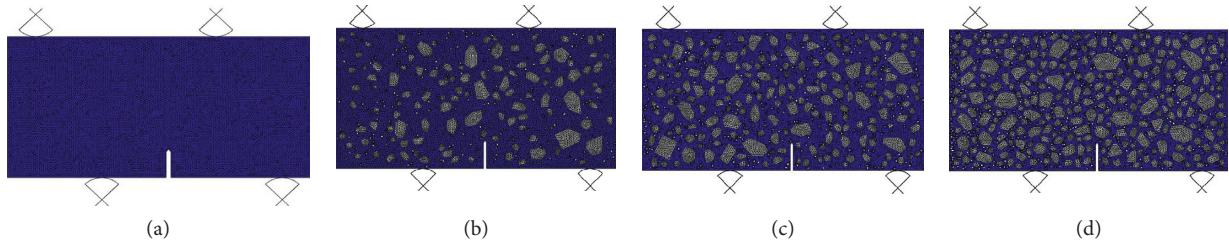


FIGURE 4: Model diagram of the volume rate of the coarse aggregate. (a)  $V_g = 0\%$ . (b)  $V_g = 29\%$ . (c)  $V_g = 48\%$ . (d)  $V_g = 68\%$ .

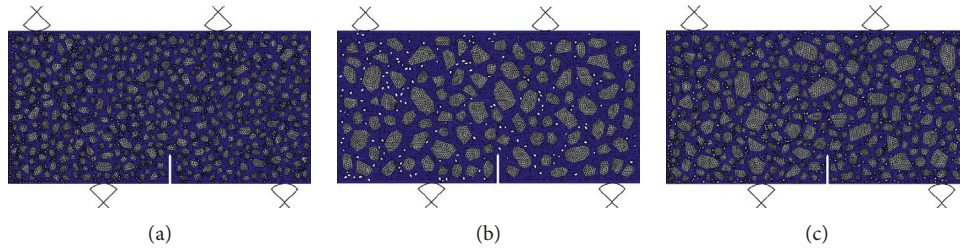


FIGURE 5: Model diagram of the maximum size of the coarse aggregate. (a)  $D_g = 9.5$  mm. (b)  $D_g = 19$  mm. (c)  $D_g = 26.5$  mm.

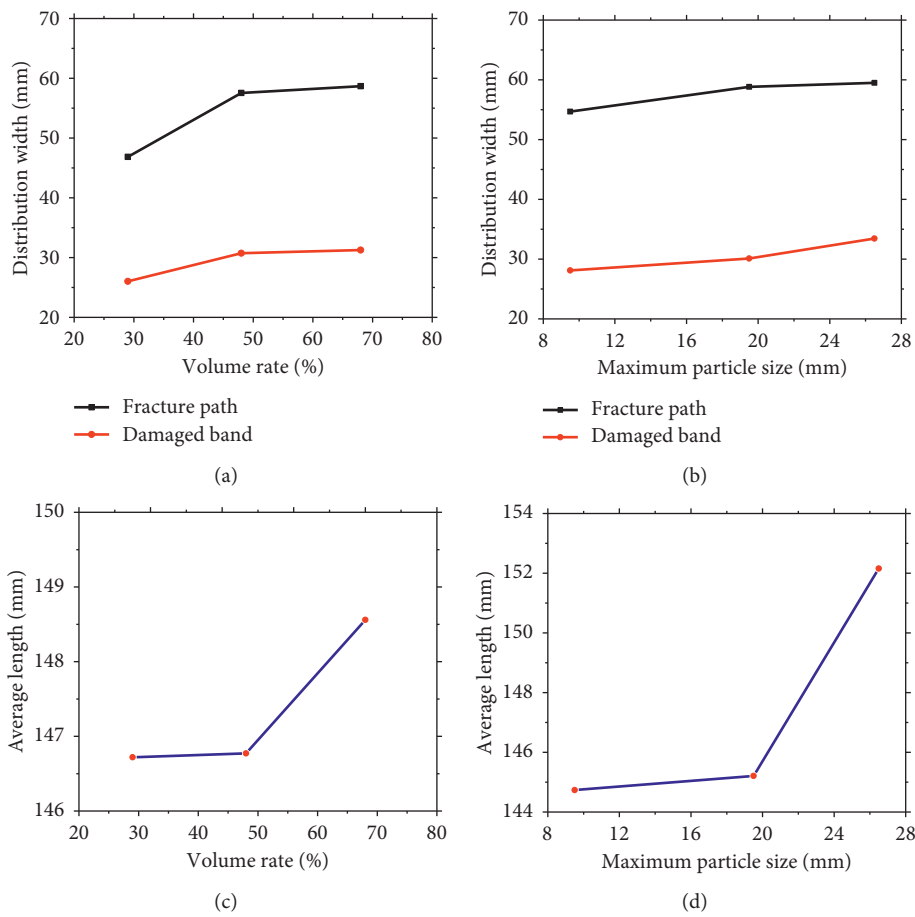


FIGURE 6: (a) The volume rate, distribution width of the fracture path, and damaged bandwidth; (b) the maximum size, distribution width of the fracture path, and damaged bandwidth; (c) the volume rate and average length of the fracture path; (d) the maximum particle size and average length of the fracture path.

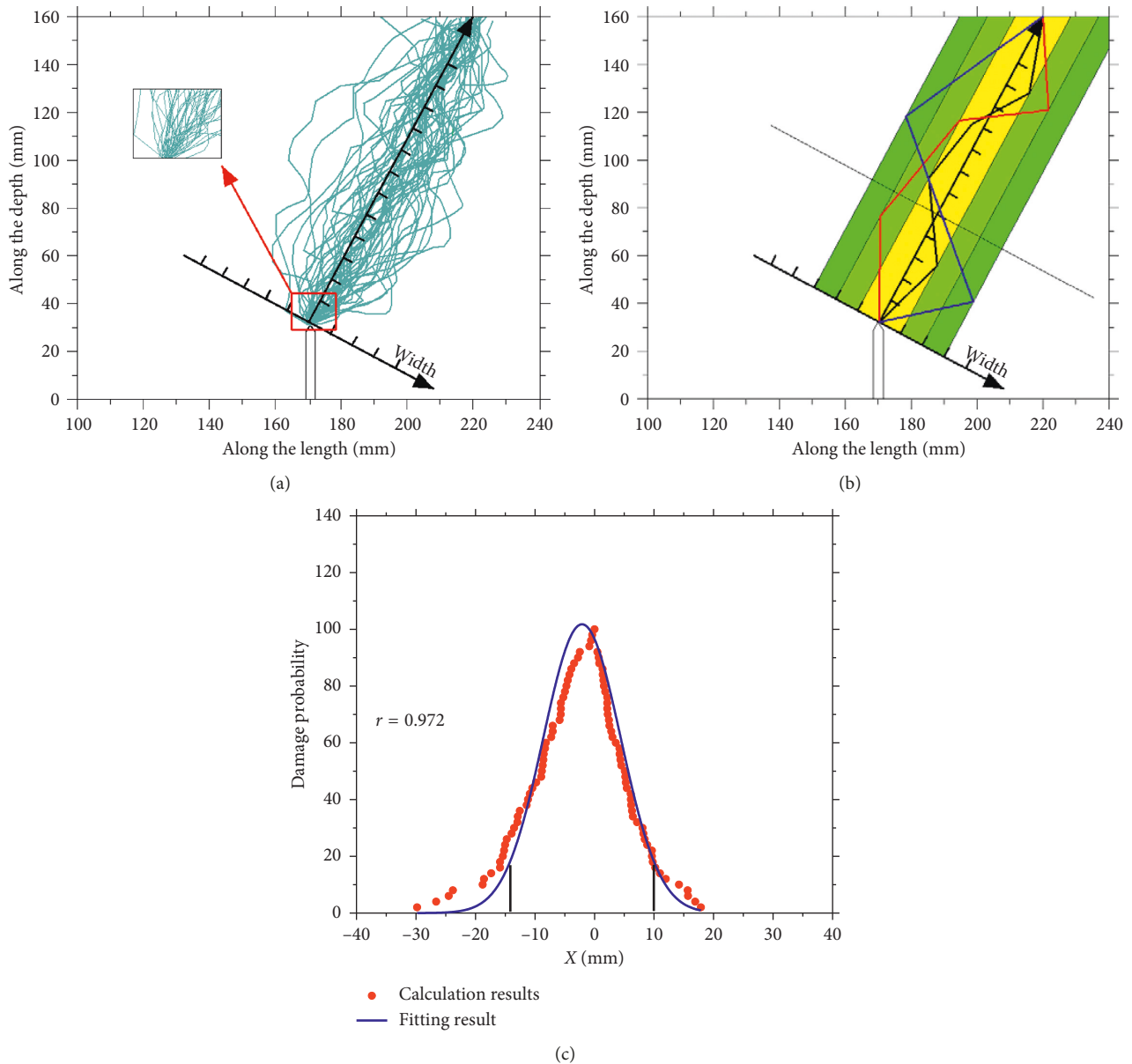


FIGURE 7: Schematic diagram of the (a) damaged bandwidth calculation, (b) damage probability calculation, and (c) damage probability calculation results.

evident that the larger the maximum size of the coarse aggregate, the wider the distribution width of the fracture path and damaged bandwidth and the more discrete the spatial distribution of the fracture path, simultaneously, the longer the average length of the fracture path, as shown in Figure 6(d). The larger the coarse aggregate maximum particle size, the fewer the coarse aggregates need to be bypassed in the process of cracks expansion (as shown in Figure 5). However, the particle size for single coarse aggregate increases obviously. In this case, the distribution width of the fracture path and the damaged bandwidth increase, and the distribution of the fracture path becomes more discrete when the cracks bypass around the coarse aggregate. Furthermore, the average length of the fracture path increases significantly with the increase of the maximum size of the coarse aggregate.

In the fracture process of concrete, the crack propagation is determined by the failure of mechanical interaction between binding materials. The coarse aggregate volume rate and the maximum particle size in concrete affect the fracture performance directly. The larger the volume rate and the maximum size of the coarse aggregate, the larger the average length and distribution width of the fracture path and the better the mechanical fracture property of concrete [28–31].

Figure 8 shows the distribution width of the fracture path for each specimen along the Y-axis in the local coordinate system of Figure 7(a). Based on the experimental results and numerical regression, the distribution height  $Y$  and the distribution width  $X$  of the fracture path are in line with the quadratic function relationship, and the fitting function and fitting results are shown in equation (10) and

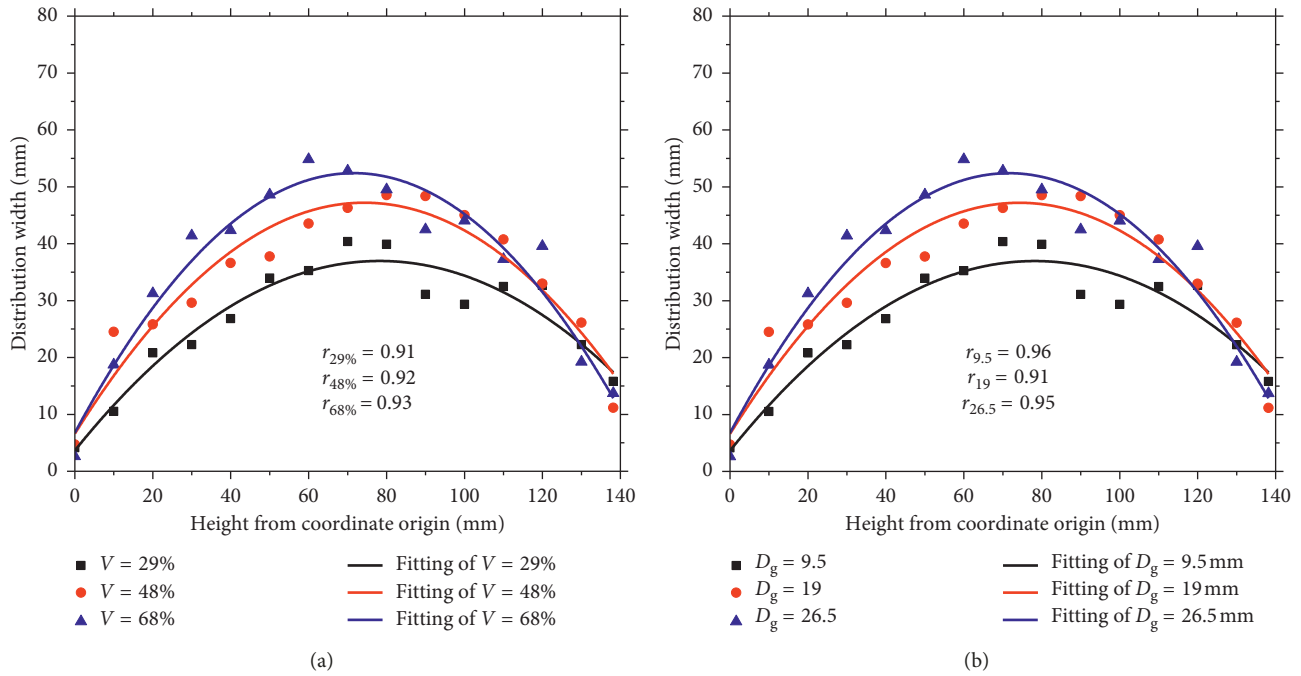


FIGURE 8: (a) The volume rate of the coarse aggregate and the distribution width of the fracture path at a different height; (b) the maximum size of the coarse aggregate and the distribution width of the fracture path at a different height.

Figure 8. The fracture path is affected by the distribution of the coarse aggregate and extends around the coarse aggregate on the failure direction. The fracture behavior of the concrete beam in the experiments is caused by the stress concentration at the top of the reserved notch and the upper middle loading point. The starting and ending positions of the fracture path are always concentrated in the vicinity of these two positions under the influence of the fracture morphology. The expansion of the fracture path is progressive, and the distribution width of the fracture path first increases and then decreases with the increases of the distribution height:

$$X = aY^2 + bY, \quad (10)$$

where  $Y$  is the distribution height of the fracture path and  $X$  represents the distribution width of the fracture path.

**4.2. Initiation Angle.** The calculation results of the pure mortar four-point shearing beam model based on the CDP model are given in Figure 9, which regards concrete as a homogeneous material composed of cement mortar. The fracture path of the pure mortar model is a straight line along the failure direction, and the grid difference causes slight deflection and bifurcation. It is found that the initiation angle of the pure cement mortar model coincides with the  $Y$ -axis in Figure 6(a) based on the statistic results of the model initiation angles. Due to the influence of the distribution for the coarse aggregate at the top of the reserved notch and the failure direction, the initiation angle of models with different volume rate and maximum sizes of the coarse aggregate is not uniform, but a discrete distribution around the failure direction. Combining with Figure 7(a), the initiation angles of the numerical simulation results distribute in the first and the second

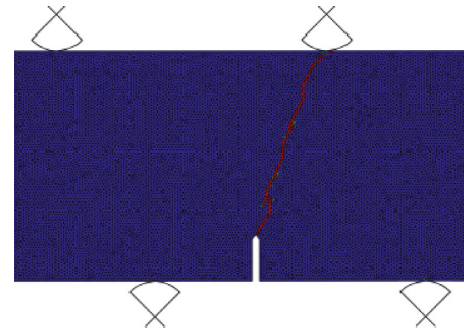


FIGURE 9: Calculation result of a pure cement mortar model.

quadrant of the local coordinate system. According to this, the first and second quadrant are expressed as  $[-90^\circ, 90^\circ]$ , the clockwise direction around the  $Y$ -axis is the positive direction of the initiation angle, and the calculation interval is divided as  $[-90^\circ, -75^\circ)$ ,  $[-75^\circ, -65^\circ)$ ,  $[-65^\circ, -55^\circ)$ , ...,  $[55^\circ, 65^\circ)$ ,  $[65^\circ, 75^\circ)$ ,  $[75^\circ, 90^\circ)$ . The distribution of the initiation angle for the simulation result is shown in Figure 10, the frequency of the distribution of the initiation angle is fitted according to the normal distribution function (equation (11)), and the correlation coefficients  $r$  of data fitting are all higher than 0.90. In this study, the standard deviation for the distribution of the initiation angle  $4\sigma$  is taken as the valid field of the initiation angle:

$$f(x) = \frac{1}{\sqrt{2\pi}\sigma} e^{-\frac{(x-\mu)^2}{2\sigma^2}}, \quad (11)$$

where  $\mu$  is the average initiation angle and  $\sigma$  is the standard deviation for the distribution of the initiation angle.

Figure 11(a) presents the valid field of the initiation angle in modes with different coarse aggregate volume rates. With

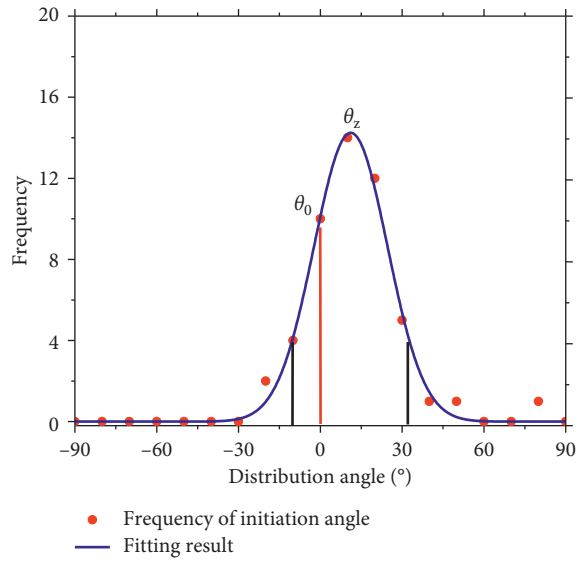


FIGURE 10: Statistical result of initiation angle.

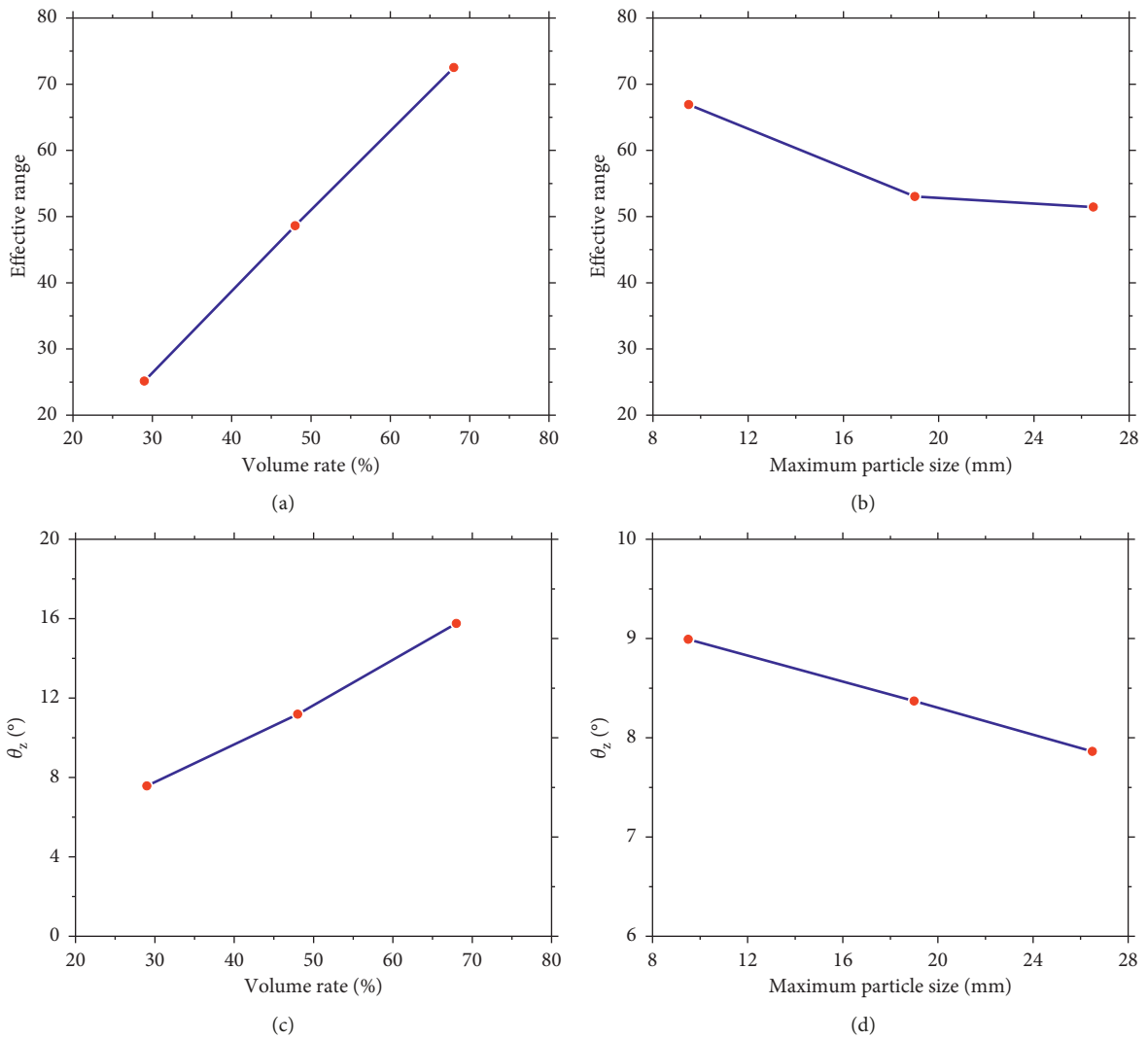


FIGURE 11: (a) Volume rate and valid field of the initiation angle; (b) maximum  $p$  size and valid field of the initiation angle; (c) volume rate and  $\theta_z$ ; (d) maximum particle size and  $\theta_z$ .

the same gradation, the valid field of the initiation angle increases with the increase of the volume rate of the coarse aggregate. The valid field is related to the standard deviation of the model initiation angle. And the amount of distribution of the coarse aggregate at the top of the reserved notch increases with the volume rate of the coarse aggregate. So the distribution of coarse aggregate become more complicated. Therefore, the dispersion degree and the valid field of the initiation angle increase. Figure 11(b) is the valid field of the initiation angle in models with different coarse aggregate maximum particle size. The valid field of the initiation angle increases with the maximum size of the coarse aggregate. The maximum size of the coarse aggregate affects the amount of the distribution of the coarse aggregate at the top of the reserved notch. The distribution of the initiation angle is more discrete with the maximum size of the coarse aggregate.

Figures 11(c) and 11(d) show the angles corresponding to the maximum distribution frequency of the initiation angle in models with coarse aggregate different volume rate and maximum particle size. And this angle is defined as the most unfavorable initiation angle  $\theta_z$  in this study. The most unfavorable initiation angle  $\theta_z$  increases with the volume rate of the coarse aggregate and decreases with the maximum size of the coarse aggregate. The amount of the coarse aggregate is positively correlated with the volume rate when the gradation keeps unchanged. The probability of the distribution of the coarse aggregate at the top of the reserved notch is more modest with the volume rate of the coarse aggregate. As a result, the most unfavorable initiation angle  $\theta_z$  is closer to it in the pure cement mortar models  $\theta_0$ . Similarly, when the volume rate of the coarse aggregate is the same, the maximum size of the coarse aggregates negatively correlated with the amount of distribution. The larger the maximum particle size of coarse aggregate is, the higher the probability of cement mortar at the top of the reserved notch and the closer the most unfavorable initiation angle  $\theta_z$  to  $\theta_0$ .

## 5. Conclusions

In this paper, the influence of volume rate and maximum size for the coarse aggregate on the fracture path and the initiation angle of mixed mode I-II fracture in concrete have been discussed at the mesolevel by the concrete damaged plasticity model and Monte Carlo simulation random aggregate method. The conclusions are as follows

- (1) In the local coordinate system, the distribution of the fracture path obeys the normal distribution function. The confidence interval and width of the distribution for the fracture path are larger with the volume rate of the coarse aggregate, and the average length of the fracture path is longer. And the confidence interval of distribution, the distribution width, and the average length of the fracture path increased with the maximum size for the coarse aggregate.
- (2) The distribution width of the fracture path first increases and then decreases with the height of the

fracture path, and it shows a quadratic parabola relationship.

- (3) The initiation angle of the pure mortar four-point shear beam model is a constant value, and the initiation angle of models with different volume rate and maximum size of the coarse aggregate obey the normal distribution function. The distribution of the coarse aggregate at the top of the reserved notch has a significant influence on the initiation angle of mixed mode I-II fracture in concrete.
- (4) The valid field of distribution for the initiation angle is larger with the volume rate of the coarse aggregate, and the most unfavorable initiation angle  $\theta_z$  is farther away from the initiation angle  $\theta_0$  of the pure cement mortar model. The valid field of distribution for the initiation angle is decreased with the increase in the maximum size of the coarse aggregate, and the value of  $\theta_z$  to the  $\theta_0$  gets closer.

## Data Availability

The data used to support the findings of this study are available from the corresponding author upon request.

## Conflicts of Interest

The authors declare that they have no conflicts of interest.

## Acknowledgments

This study was supported by the National Natural Science Foundation of China (51568053).

## References

- [1] P. Cao, D. Feng, C. Zhou, and W. Zuo, "Study on fracture behavior of polypropylene fiber reinforced concrete with bending beam test and digital speckle method," *Computers and Concrete*, vol. 14, no. 5, pp. 527–546, 2014.
- [2] J. Pan, Y. T. Feng, F. Jin et al., "Meso-scale particle modeling of concrete deterioration caused by alkali-aggregate reaction," *International Journal for Numerical and Analytical Methods in Geomechanics*, vol. 37, no. 16, pp. 2690–2705, 2013.
- [3] K. P. Vishalakshi, V. Revathi, and S. Sivamurthy Reddy, "Effect of type of coarse aggregate on the strength properties and fracture energy of normal and high strength concrete," *Engineering Fracture Mechanics*, vol. 194, pp. 52–60, 2018.
- [4] W. Dong, Z. Wu, X. Tang, and X. Zhou, "A comparative study on stress intensity factor-based criteria for the prediction of mixed mode I-II crack propagation in concrete," *Engineering Fracture Mechanics*, vol. 197, pp. 217–235, 2018.
- [5] T. Liu, S. Qin, D. Zou, W. Song, and J. Teng, "Mesoscopic modeling method of concrete based on statistical analysis of CT images," *Construction and Building Materials*, vol. 192, pp. 429–441, 2018.
- [6] R. Pullin, M. Baxter, M. J. Eaton, K. M. Holford, and S. L. Evans, "Novel acoustic emission source detection," *Journal of Acoustic Emission*, vol. 25, pp. 215–223, 2007.
- [7] J. Hensman, R. Mills, S. G. Pierce, K. Worden, and M. Eaton, "Locating acoustic emission sources in complex structures

- using Gaussian processes,” *Mechanical Systems and Signal Processing*, vol. 24, no. 1, pp. 211–223, 2010.
- [8] X. Yang and F. Wang, “Random-fractal-method-based generation of meso-model for concrete aggregates,” *Powder Technology*, vol. 284, no. 14, pp. 63–77, 2015.
- [9] B. Chen and J. Liu, “Effect of aggregate on the fracture behavior of high strength concrete,” *Construction and Building Materials*, vol. 18, no. 8, pp. 585–590, 2004.
- [10] J. Xiao, H. Schneider, C. Dönnecke, and G. König, “Wedge splitting test on fracture behaviour of ultra high strength concrete,” *Construction and Building Materials*, vol. 18, no. 6, pp. 359–365, 2004.
- [11] M. H. A. Beygi, M. T. Kazemi, I. M. Nikbin, J. Vaseghi Amiri, S. Rabbanifar, and E. Rahmani, “The influence of coarse aggregate size and volume on the fracture behavior and brittleness of self-compacting concrete,” *Cement and Concrete Research*, vol. 66, pp. 75–90, 2014.
- [12] M. H. A. Beygi, M. T. Kazemi, J. Vaseghi Amiri, I. M. Nikbin, S. Rabbanifar, and E. Rahmani, “Evaluation of the effect of maximum aggregate size on fracture behavior of self-compacting concrete,” *Construction and Building Materials*, vol. 55, pp. 202–211, 2014.
- [13] M. Ghasemi, M. R. Ghasemi, and S. R. Mousavi, “Investigating the effects of maximum aggregate size on self-compacting steel fiber reinforced concrete fracture parameters,” *Construction and Building Materials*, vol. 162, pp. 674–682, 2018.
- [14] B. Ackay, A. S. Agar-Ozbek, F. Bayramov, H. N. Atahan, C. Sengul, and M. A. Tasdemir, “Interpretation of aggregate volume fraction effects on fracture behaviour of concrete,” *Construction and Building Materials*, vol. 28, no. 1, pp. 437–443, 2012.
- [15] G. Li, J. Yu, P. Cao, and Z. Ren, “Experimental and numerical investigation on I-II mixed-mode fracture of concrete based on the Monte Carlo random aggregate distribution,” *Construction and Building Materials*, vol. 191, pp. 523–534, 2018.
- [16] C. Peng, L. Guodong, Y. Jiangjiang, Z. Ming, J. Feng, and Z. Zhimeng, “Research and application of random aggregate model in determining the fracture behavior of four-point bending beam with notch,” *Construction and Building Materials*, vol. 202, pp. 276–289, 2019.
- [17] J. Lee and L. G. Fenves, “Plastic-damage model for cyclic loading of concrete structures,” *Journal of Engineering Mechanics*, vol. 124, no. 8, pp. 892–900, 1998.
- [18] J. Lee and G. L. Fenves, “A plastic-damage concrete model for earthquake analysis of dams,” *Earthquake Engineering & Structural Dynamics*, vol. 27, no. 9, pp. 937–956, 1998.
- [19] A. J. Aref and K. M. Dolatshahi, “A three-dimensional cyclic meso-scale numerical procedure for simulation of unreinforced masonry structures,” *Computers & Structures*, vol. 120, pp. 9–23, 2013.
- [20] Y. Huang, Z. Yang, W. Ren, G. Liu, and C. Zhang, “3D meso-scale fracture modelling and validation of concrete based on in-situ X-ray computed tomography images using damage plasticity model,” *International Journal of Solids and Structures*, vol. 67–68, pp. 340–352, 2015.
- [21] X. Du, L. Jin, and G. Ma, “Numerical simulation of dynamic tensile-failure of concrete at meso-scale,” *International Journal of Impact Engineering*, vol. 66, pp. 5–17, 2014.
- [22] G. M. Chen, J. F. Chen, and J. G. Teng, “On the finite element modelling of RC beams shear-strengthened with FRP,” *Construction and Building Materials*, vol. 32, pp. 13–26, 2012.
- [23] G. H. Mahmud, Z. Yang, and A. M. T. Hassan, “Experimental and numerical studies of size effects of ultra high performance steel fibre reinforced concrete (UHPFRC) beams,” *Construction and Building Materials*, vol. 48, pp. 1027–1034, 2013.
- [24] G. M. Chen, J. G. Teng, and J. F. Chen, “Finite-element modeling of intermediate crack debonding in FRP-plated RC beams,” *Journal of Composites for Construction*, vol. 15, no. 3, pp. 339–353, 2011.
- [25] J. Lubliner, J. Oliver, S. Oller, and E. Oñate, “A plastic-damage model for concrete,” *International Journal of Solids and Structures*, vol. 25, no. 3, pp. 299–326, 1989.
- [26] N. F. Hany, E. G. Hantouche, and M. H. Harajli, “Finite element modeling of FRP-confined concrete using modified concrete damaged plasticity,” *Engineering Structures*, vol. 125, pp. 1–14, 2016.
- [27] C. Farahmandpour, S. Dartois, M. Quiertant, Y. Berthaud, and H. Dumontet, “A concrete damage-plasticity model for FRP confined columns,” *Materials and Structures*, vol. 50, p. 156, 2017.
- [28] D. G. Zollinger, T. Tang, and R. H. Yoo, “Fracture toughness of concrete at early stages,” *ACI Materials Journal*, vol. 90, no. 5, pp. 463–471, 1993.
- [29] I. M. Nikbin, M. H. A. Beygi, M. T. Kazemi et al., “Effect of coarse aggregate volume on fracture behavior of self-compacting concrete,” *Construction and Building Materials*, vol. 52, pp. 137–145, 2014.
- [30] M. Karamloo, M. Mazloom, and G. Payganeh, “Effects of maximum aggregate size on fracture behaviors of self-compacting lightweight concrete,” *Construction and Building Materials*, vol. 123, pp. 508–515, 2016.
- [31] Y. Wang and X. Hu, “Determination of tensile strength and fracture toughness of granite using notched three-point-bend samples,” *Rock Mechanics and Rock Engineering*, vol. 50, no. 1, pp. 1–12, 2017.

